

CATALYSIS

Nickel promotes selective ethylene epoxidation on silver

Anika Jalil^{1†}, Elizabeth E. Happel^{2†}, Laura Cramer^{2†}, Adrian Hunt³, Adam S. Hoffman^{4,5}, Iradwikanari Waluyo³, Matthew M. Montemore^{6*}, Phillip Christopher^{1*}, E. Charles H. Sykes^{2,7*}

Over the last 80 years, chlorine (Cl) has been the primary promoter of the ethylene epoxidation reaction valued at ~40 billion USD per year, providing a ~25% selectivity increase over unpromoted silver (Ag) (~55%). Promoters such as cesium, rhenium, and molybdenum each add a few percent of selectivity enhancements to achieve 90% overall, but their codependence on Cl makes optimizing and understanding their function complex. We took a theory-guided, single-atom alloy approach to identify nickel (Ni) as a dopant in Ag that can facilitate selective oxidation by activating molecular oxygen (O₂) without binding oxygen (O) too strongly. Surface science experiments confirmed the facile adsorption/desorption of O₂ on NiAg, as well as demonstrating that Ni serves to stabilize unselective nucleophilic oxygen. Supported Ag catalyst studies revealed that the addition of Ni in a 1:200 Ni to Ag atomic ratio provides a ~25% selectivity increase without the need for Cl co-flow and acts cooperatively with Cl, resulting in a further 10% initial increase in selectivity.

Ethylene oxide [(EO) C₂H₄O] is a platform chemical in the production of many consumer goods including plastics and anti-freeze, with a growing global market currently valued at ~40 billion USD per year (1). It is produced from ethylene (C₂H₄) and molecular oxygen (O₂) using Ag/ α -alumina (α -Al₂O₃) heterogeneous catalysts. Because of the instability of EO, industrial reactors are operated at only ~10 to 15% per-pass ethylene conversion to minimize combustion of EO into CO₂ and H₂O (2).

The low per-pass conversion, low reactant partial pressures (>50% of the feed is inert to mitigate thermal runaway), and high production volumes all necessitate large-volume recycle streams. These energy-intensive separation processes add to the 10% CO₂ emitted as a by-product of the 90% selective EO production process, so EO has the highest CO₂ emission among high-value chemicals on a per volume basis (3). Thus, even small improvements in EO selectivity could lead to large decreases in associated CO₂ emissions and energy costs, making the design of selective EO production catalysts a subject of continued interest (4, 5).

Achieving high EO selectivity requires minimizing both the direct combustion of ethylene and the secondary combustion of EO to CO₂.

The relatively high fraction of EO produced over silver (Ag) catalysts has been widely attributed to its oxygen adsorption properties (6–8). Ag/ α -Al₂O₃ catalysts exhibit ~50 to 60% EO selectivity at <10% ethylene conversion, although selectivity decreases with increasing ethylene conversion through EO combustion.

Despite safety issues and environmental impacts in addition to its corrosive nature, chlorine (Cl) is used ubiquitously to promote the selectivity of industrial EO catalysts which consist of large (50 nm to 1 μ m diameter) Ag particles supported on low surface area (<1 m²/g) α -Al₂O₃. Chlorine is co-fed as an alkyl chloride and increases EO selectivity by ~25% at low ethylene conversion compared with pure Ag/ α -Al₂O₃, and enables EO selectivity to be retained at higher conversion (9), which suggests that Cl promotes EO formation by depressing the rates of both the primary and secondary combustion reactions (9–11).

Other promoters of industrial EO catalysts include alkali metals such as cesium (Cs) and lithium (Li), and oxyanions of transition metals such as molybdenum (Mo) and rhenium (Re), which each offer modest ~1 to 5% increases in EO selectivity but require the presence of Cl to be effective. Furthermore, promoters can be codependent on one another. For example, Re only increases selectivity in the presence of Cs, which itself requires Cl. These requirements make the system complex, as the addition of parts per million (ppm) levels of alkyl chloride and other promoters (promoter: Ag molar ratios of 10⁻⁴–10⁻²) required for ~90% EO selectivity at 10 to 15% ethylene conversion results in crowded, multicomponent catalytic surfaces (12–16).

Promoters are thought to influence the amount, accessibility, and reactivity of oxygen species (9, 14, 17–22). The ubiquity of Cl as a promoter in most catalyst formulations has

limited research on identification of new promoters that act independently of Cl. A few reports exist of modest (5 to 10%) selectivity increases by using unconventional (not currently used in industrial formulations) promoters, but high EO selectivity at reasonable ethylene conversion remains a challenge without Cl (23–25).

We report that the addition of parts per million amounts of Ni to supported Ag catalysts substantially enhanced EO selectivity by ~25%, rivaled only by the ubiquitously used Cl promoter. Our theoretical and experimental surface science studies demonstrate that dispersed Ni in Ag(111) simultaneously influenced the quantity and reactivity of adsorbed oxygen species. Catalytic studies revealed that dilute Ni promoters (at 200:1 Ag:Ni ratio) on supported Ag/ α -Al₂O₃ catalysts function synergistically with Cl feeds to enable 90% EO selectivity at 2 to 2.5% ethylene conversion, indicating that Ni offers a new avenue for catalyst and process optimization in EO production.

Theory-guided catalyst discovery

We initially searched for promoters for Ag-based EO-producing catalysts using our single-atom alloy (SAA) approach that has identified new selective (de)hydrogenation catalysts, including rhodium (Rh), platinum (Pt), and palladium (Pd) doped copper (Cu) SAAs (26–29). These catalysts derive their function from the facile dissociation of strong bonds and weak binding of intermediates enabled by the SAA geometry that can decouple transition and final state energies. We applied this concept to selective oxidations using density functional theory (DFT) calculations to identify single-atom dopants in Ag surfaces with a low dissociative oxygen chemisorption activation barrier ($E_{a,diss}$) and weak atomic oxygen binding energy when bound in hollow sites on each side of the dopant site ($E_{ads,2O}$; fig. S2) as shown in Fig. 1A (6). Among the screened dopants, Ni stood out as breaking the scaling relationship (fig. S1) between $E_{a,diss}$ and $E_{ads,2O}$, with DFT predicting near-barrierless dissociation of O₂ (<0.05 eV) while maintaining moderate atomic oxygen atom binding (~2.2 eV) (30).

Surface adsorption experiments

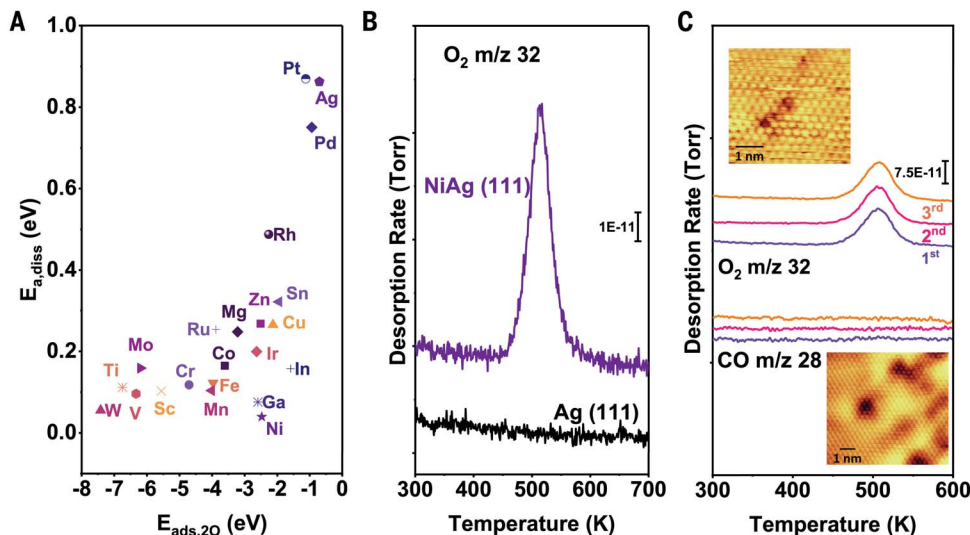
To test this prediction, we conducted surface-science studies of O₂ activation on 1% Ni-doped Ag(111) single-crystal surfaces. In these experiments, 1% monolayer (ML) of Ni was alloyed into the Ag(111) surface to obtain dispersed Ni in the surface and subsurface (Fig. 1C and S5). The dissociative sticking probability of O₂ on Ag(111) is ~10⁻⁶ which requires high O₂ pressures in the Torr range, or a more reactive oxidant such as NO₂, to saturate the surface with atomic oxygen (31, 32). However, Fig. 1B shows that the addition of 1% monolayer (ML) Ni to Ag(111) enabled uptake of oxygen on Ag at 10⁻⁶ Torr pressure of O₂.

¹Department of Chemical Engineering, University of California, Santa Barbara, CA, USA. ²Department of Chemistry, Tufts University, Medford, MA, USA. ³National Synchrotron Light Source II, Brookhaven National Laboratory, Upton, NY, USA. ⁴Stanford Synchrotron Radiation Light Source, SLAC National Accelerator Laboratory, Menlo Park, CA, USA. ⁵SUNCAT Center for Interfacial Science and Catalysis, SLAC National Accelerator Laboratory, Menlo Park, CA, USA. ⁶Department of Chemical and Biomolecular Engineering, Tulane University, New Orleans, LA, USA. ⁷Department of Chemical and Biological Engineering, Tufts University, Medford, MA, USA.

*Corresponding author. Email: mmontemore@tulane.edu (M.M.M.); pchristopher@uconn.edu (P.C.); charles.sykes@tufts.edu (E.C.H.S.)

†These authors contributed equally to this work.

Fig. 1. Theory-guided identification of Ni dopant that enables facile O₂ dissociation and spillover of oxygen to Ag. (A) DFT calculations of the O₂ dissociation barrier $E_{a,diss}$ as a function of the adsorption energy of the resulting dissociated O atoms ($E_{ads,2O}$) for various single-atom dopants in Ag(111). (B) O₂ TPD traces for Ag(111) and ~1% NiAg(111) after 500 Langmuirs (L) of O₂ dosed at 350 K, cooling to room temperature, and recording the TPD with a 1 K/s heating rate. (C) Sequential TPD traces involving a 500 L exposure to O₂ at 350 K and TPD, followed by 0.5 L CO exposure at 90 K and TPD. Insets show 13 K STM images of subsurface Ni in Ag(111) immediately after Ni deposition (lower image, image conditions 0.2 nA, 100 mV) and Ni at the surface of Ag(111) after cooling from 473 K in O₂ (upper image, 0.3 nA, 50 mV).



Specifically, the NiAg(111) sample was exposed to 500 L (1 L = 1×10^{-6} Torr/sec) of O₂ at 350 K. Temperature-programmed desorption (TPD) of adsorbed oxygen demonstrates facile uptake and spillover of the dissociated oxygen atoms to sites on Ag(111). Calibration of the trace in Fig. 1B indicated that 1% ML Ni enabled the uptake of ~4% ML O. Furthermore, O₂ desorbed from NiAg at 520 K. This temperature is ~70 K lower than typically observed from pure Ag (Fig. 1B) and consistent with our DFT prediction (Fig. 1A and table S1) of promoted O₂ uptake and release by Ni dopants (31, 33).

Consecutive CO and O₂ adsorption TPDs demonstrated that the Ni atoms were mobile within the Ag sample. The Ni atoms were in the Ag(111) surface under oxidizing conditions but moved to the subsurface under vacuum conditions (Fig. 1C). Specifically, we used CO as a probe molecule to measure the surface concentration of Ni. Although CO does not bind to Ag(111) above ~50 K, the introduction of Ni to Ag(111) led to observation of a CO desorption peak at ~350 K (fig. S6) (34). This CO desorption temperature is ~80 K lower than that observed for Ni(111) and is further evidence of the high dispersion of Ni in Ag(111) (35).

After O₂ exposure and subsequent TPD, we exposed the NiAg surface to 0.5 L of CO, but no CO desorption was observed in TPD. This result indicated that Ni moved to the subsurface by the end of the O₂ desorption TPD ramp to 700 K. Subsequent exposure to O₂ brought Ni back to the surface. This preference is expected based on the more oxophilic nature of Ni, and the reversibility of Ni surface segregation over three full cycles is shown in Fig. 1C.

Nanoparticle catalysts for epoxidation

To determine if the surface-science and theoretical studies could be translated to supported

catalysts, we synthesized highly dilute NiAg nanoparticle alloys and compared their performance in ethylene epoxidation with pure Ag/ α -Al₂O₃ catalysts (Fig. 2). Ag nanoparticles ~70 nm in diameter were synthesized (figs. S4, S7, and S8) with varying Ni content through a colloidal approach. This particle size was chosen because smaller (5 to 50 nm) and larger (>250 nm) diameter Ag particles exhibit lower reaction rates, and smaller Ag particles are prone to rapid sintering (11, 36–38). The Ag nanoparticles were post synthetically doped with Ni to ensure a constant Ag particle size distribution (39, 40).

Our TPD results showing Ni mobility and segregation to the surface after O₂ exposure emphasized that under ethylene epoxidation reaction conditions, the oxophilicity of Ni should provide a thermodynamic driving force for Ni to move to the Ag nanoparticle surface. Further, the reaction temperature (473 to 523 K) is high enough to kinetically enable Ni to segregate to the surface as observed in TPD when Ni diffusion to the surface occurred at 350 K. Therefore, to calculate nominal Ni surface coverage, we made the simplifying assumption that all the Ni in a nanoparticle resided at the Ag surface when O₂ is present. This allowed us to calculate a range of target Ni:Ag ratios for the synthesis, assuming spherical nanoparticles (fig. S7). We then synthesized catalysts with Ni loadings ranging from 1:500 (0.2 mol%) to 1:50 (2 mol%) which corresponded to 10 and 80% estimated Ni surface coverage, respectively. It should be noted that this is an upper limit as the thermodynamics of Ni partitioning between the bulk and surface is dependent on particle size and environmental conditions.

Catalysts were characterized with a variety of techniques (figs. S8 to S11, S14 to S17, and

tables S2 to S4). Inductively coupled plasma (ICP) measurements showed that the desired Ni loadings were achieved (table S4). Ni K-edge high-energy resolution fluorescence detection-X-ray absorption near-edge structure (HERFD-XANES) spectroscopy measurements were collected for an as-prepared 9 weight percent (wt%) NiAg₂₀₀/ α -Al₂O₃ catalyst and for ~5 nm NiO particles on α -Al₂O₃ (figs. S14 to S16) during a temperature programmed reduction (TPR). Linear-combination fitting of the NiO TPR produced negligible residuals, demonstrating that the spectra were fit well using NiO and reduced Ni nanoparticle basis sets (figs. S15 and S16A). The spectrum of the as-prepared NiAg₂₀₀ samples was poorly fit by the same basis set. The different electronic structure and local coordination environment of Ni in NiAg₂₀₀ compared with pure Ni on α -Al₂O₃, evidenced by HERFD-XANES, indicated that the synthetic procedure effectively incorporated Ni in Ag and is different from pure dispersed Ni on α -Al₂O₃.

Steady-state reactivity experiments were performed with a feed of 10% ethylene and 10% molecular oxygen (at 1 bar in 80% inert) at 473, 498, and 523 K. Ni-doped 5 wt% Ag/ α -Al₂O₃ (NiAg₅₀/ α -Al₂O₃) catalysts with stoichiometries ranging from NiAg₅₀₀ to NiAg₅₀ were all prepared from the same parent batch of Ag colloids (see figs. S18 and S20 and table S5 for details on the reactivity protocols). Steady-state ethylene conversion for Ag/ α -Al₂O₃ was varied from 2 to 8% with 100 to 150 mg of catalyst in the reactor by varying the reaction temperature (Fig. 2A).

The EO selectivity for Ag/ α -Al₂O₃, calculated as $\frac{N_{EO}}{N_{EO} + 0.5N_{CO_2}}$, where N_i is the molar flow rate of each species, decreased from 50 to 30% as conversion increased, consistent with previous reports (table S6) (36, 41–43). The addition of just 1:350 Ni:Ag (0.3 atom percent of

Ni) to Ag resulted in an increase in EO selectivity by 5 to 10% at all conversions. Increasing the Ni loading further increased EO selectivity and decreased ethylene conversion. NiAg₂₀₀ appeared to be the optimum Ni content for this batch of Ag particles, which exhibited a 25 to 30% increase in selectivity over Ag, comparable to the known behavior of Cl promoters. Figure S12 shows the effect of increasing Ni loading on selectivity at 2% ethylene conversion revealing a maximum selectivity at a 1:200 Ni:Ag molar ratio which improves EO selectivity by ~25% over pure Ag. The selectivity at low conversion (< 2%) can be considered the primary selectivity (at the limit of low EO combustion rate), and at higher ethylene conversions, the rate of secondary EO combustion is relevant. Thus, the results in Fig. 2A demonstrate that 1:200 Ni:Ag (0.5% Ni) mitigated both primary ethylene and secondary EO combustion. At Ni loadings higher than NiAg₂₀₀, both selectivity and conversion decreased, suggesting that extended NiO_x domains may block reactive sites on Ag and further facilitate EO combustion (see fig. S19).

Increasing the Ni loading led to a decrease in CO₂ production rate whereas the EO production rate decreased to a lesser degree, resulting in overall increased EO selectivity (Fig. 2, B and C). The ethylene conversion at 473 K was <2% and thus the CO₂ and EO production (as shown in Fig. 2, B and C) demonstrates the influence of Ni on the primary reaction pathways (conversion of ethylene to CO₂ or EO). At 523 K, where ethylene conversion was higher and the secondary reaction of EO combustion was likely more prevalent, the depression in CO₂ production rates with Ni addition was clearly observed with no change (or even a small increase) in EO production rates. The larger influence of Ni incorporation on selectivity at higher temperatures supported the conclusion that Ni suppressed secondary EO combustion while also promoting primary selectivity. Notably, the trends in selectivity and rates of product formation as a function of Ni concentration were similar to how Cl performs as a promoter (fig. S13).

The NiAg₂₀₀ formulation offered consistent performance improvement over Ag catalyst samples across multiple catalyst syntheses. The magnitude and statistical significance of the optimal Ni loading was quantified by comparing the reactivity of seven independently prepared batches of Ag/ α -Al₂O₃ and NiAg₂₀₀/ α -Al₂O₃ at an ~8 wt% Ag loading. The temperature, catalyst loading, and total flow rate were varied to compare EO selectivity at a broad range of ethylene conversions. Figure 3A shows that even with batch-to-batch performance variation, NiAg₂₀₀ repeatedly improved EO selectivity by at least 20% over a broad range of ethylene conversions up to 10%.

To explore the promoting influence of Ni at more industrially relevant reaction conditions,

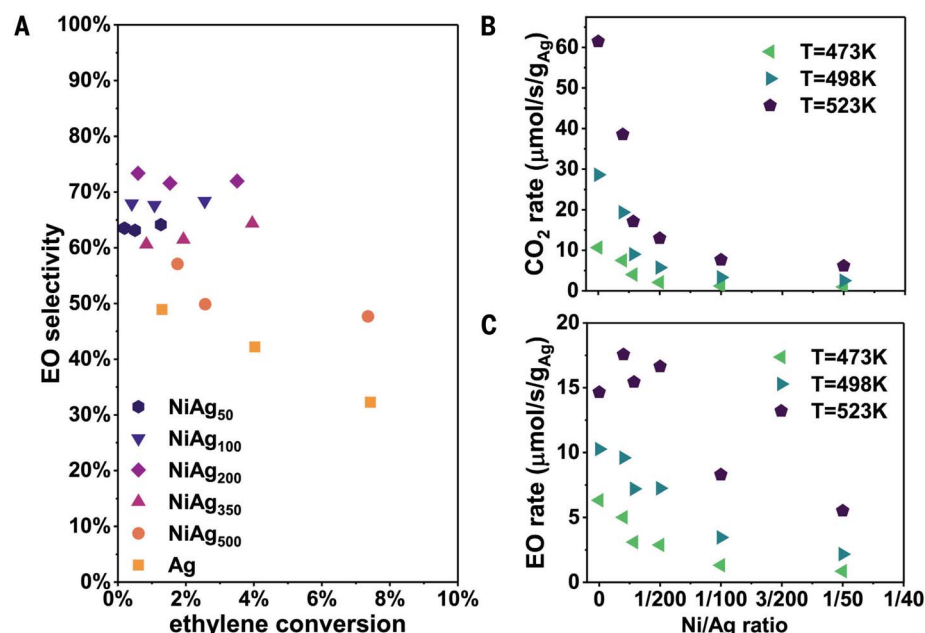


Fig. 2. Ni doping of Ag nanoparticles at a molar ratio of 1:200 Ni:Ag increases EO selectivity by ~25% compared with pure Ag. Influence of Ni loading on 5 wt% Ag/ α -Al₂O₃ catalyst reactivity in 10% C₂H₄, 10% O₂, balance He inlet with 100 to 150 mg catalyst. The Ni:Ag molar ratio was varied from 0:100 (pure Ag) to 1:50 (2% Ni). (A) EO selectivity as a function of steady-state ethylene conversion. The ethylene conversion was varied by changing the temperature between 473, 498, and 523 K, and holding for 2 hours to allow the system to reach a new steady state. (B) CO₂ and (C) EO formation rates at different temperatures as a function of Ni:Ag molar ratio.

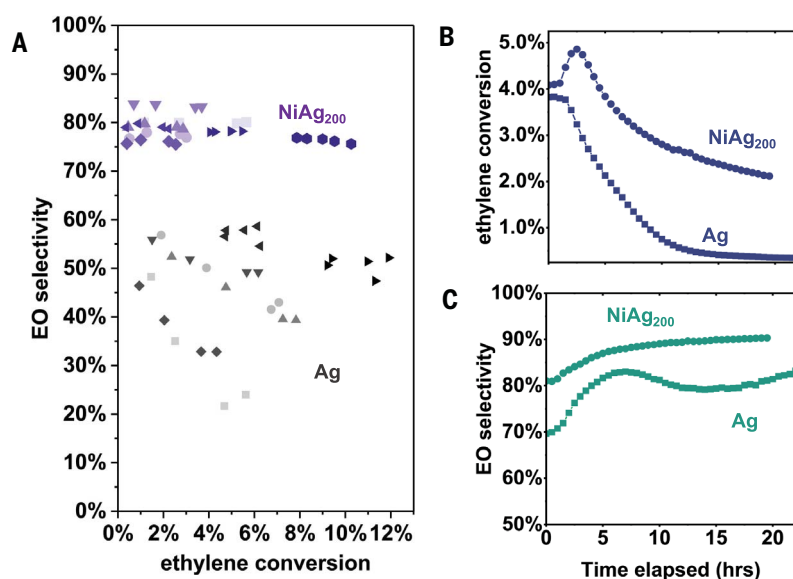


Fig. 3. NiAg₂₀₀ catalysts show a consistent ~25% selectivity enhancement over Ag and additive influence of Cl co-promoter. (A) EO selectivity as a function of ethylene conversion for seven batches of ~8 wt% Ag and NiAg₂₀₀ on α -Al₂O₃ at 10% C₂H₄, 10% O₂, balance He. The reactivity of separate batches is shown by using various shades of purple (NiAg₂₀₀) and gray (Ag). See table S5 for details on all samples. (B and C) Effect of Cl co-flow at 25% C₂H₄, 10% O₂, 0.5% CO₂, and 0.5 ppm EtCl, balance He (total flow rate 40 standard cubic centimeters per minute) at 523 K: (B) NiAg₂₀₀ and Ag ethylene conversion (see fig. S21 for product formation rates over time) and corresponding (C) NiAg₂₀₀ and Ag selectivity.

a feed composition containing 25% C₂H₄, 10% O₂, 0.5% CO₂, and 0.5 ppm ethyl chloride (EtCl) was used (44). Although the conversion of Ag/ α -Al₂O₃ declined substantially with time upon

Cl introduction, decreasing from 3.8 to 0.3% in 18 hours (Fig. 3B and fig. S21A), the selectivity increased from 68% to 82% (Fig. 3C). NiAg₂₀₀ had a comparatively lower decrease in rates

($\sim 2\times$ as compared to $>10\times$ for Ag) after an initial increase in reactivity, with selectivity increasing to just $>90\%$. The initial increase in EO formation rate for NiAg₂₀₀ and lower decrease in rate due to Cl introduction (fig. S21B) suggested that Ni and Cl were interacting on the Ag surface to modify the epoxidation pathways, which further supports the hypothesis that Ni is incorporated directly into the Ag nanoparticles rather than being located on the support. We note that optimized performance of Cl with other promoters is known to require co-optimization as a function of reaction conditions, suggesting that further improvements in performance are possible.

Ambient-pressure surface spectroscopy

Ambient-pressure x-ray photoelectron spectroscopy (AP-XPS) experiments demonstrated that the addition of Ni stabilized nucleophilic oxygen, which is generally believed to be responsible for non-selective primary and secondary combustion reactions on the Ag surface (45). Specifically, exposure of both Ag(111) and NiAg(111) surfaces to 1 Torr O₂ at 325 K led primarily to the formation of electrophilic (~ 530.2 eV) and nucleophilic (~ 528.5 eV) oxygen species (Fig. 4). The NiAg sample exhibited an additional O 1s peak at 529.3 eV (blue trace, Fig. 4B), consistent with a Ni-O species (labeled as “Ni-philic”; table S7) (46). Apart from the presence of the Ni-philic oxygen spe-

cies on the NiAg(111) sample, both the Ag(111) and NiAg(111) surfaces behave similarly from 325 to 550 K: as the surface temperature is raised, the electrophilic oxygen is seen converting to nucleophilic oxygen on both surfaces. However, it is clear from Fig. 4B that on the NiAg surface nucleophilic oxygen persists up to 700 K versus 550 K on Ag(111). We hypothesize that this increased thermal stability of the nucleophilic oxygen induced by Ni incorporation should decrease its reactivity, lowering the non-selective primary and secondary combustion rates thereby enhancing EO selectivity compared with the Ni-free system, as seen in the catalytic measurements. Our DFT calculations show that Ni stabilizes nucleophilic O on Ag (fig. S3), rendering the nucleophilic oxygen which typically drives combustion more “spectator-like,” and less reactive to ethylene combustion (47).

Our reactivity data in Fig. 3 also support this hypothesis in that the addition of Ni to Ag decreased the combustion rate more than the EO formation rate, providing a coherent picture of the proposed mechanism whereby Ni decreases unselective reactions of ethylene and EO with nucleophilic oxygen by stabilizing the O atoms in the structure. Further studies are aimed at developing scalable synthetic protocols on low surface area supports that further increase EO selectivity by minimizing secondary combustion sites for operation at higher reactor pressures.

Discussion

Guided by theory and experimental surface science results, we synthesized and tested dilute Ni-doped Ag nanoparticles and found an EO selectivity increase of $\sim 25\%$ compared with pure Ag, a promotion magnitude previously only achievable with a co-flow of Cl. Our study identified dilute ($\sim 1:200$) Ni:Ag alloys as an optimal concentration for promoting selective EO formation on ~ 75 nm Ag nanoparticles, and the addition of Cl was found to further promote the selectivity of NiAg to $\sim 90\%$ without the need for promoters like Cs and Re that are normally required to reach this selectivity. Our AP-XPS results suggest that the $\sim 25\%$ selectivity enhancement results from Ni-induced stabilization of nucleophilic oxygen on the Ag surface, thereby decreasing the rates of ethylene and EO combustion. Overall, this study highlights the potential of theory-led exploration in dilute alloy materials space and the utility of our single-atom alloy approach for the design of selective oxidation catalysts.

REFERENCES AND NOTES

- Ethylene Oxide and Ethylene Glycol Market by Product and Geography - Forecast and Analysis 2021-2025. (Technavio, 2021); <https://www.technavio.com/report/ethylene-oxide-and-ethylene-glycol-market-industry-analysis>.
- J. H. Miller, A. Joshi, X. Li, A. Bhan, *J. Catal.* **389**, 714–720 (2020).
- IEA, Technology Roadmap - Energy and GHG Reductions in the Chemical Industry via Catalytic Processes. (IEA Report, 2013); <https://www.iea.org/reports/technology-roadmap-energy-and-ghg-reductions-in-the-chemical-industry-via-catalytic-processes>.
- Shell Global, Ethylene Oxide Catalysts. (Shell, 2025); <https://www.shell.com/business-customers/catalysts-technologies/catalysts/petrochemical-catalysts/ethylene-oxide-catalysts.html>.
- C. Stegelmann, N. C. Schiadt, C. T. Campbell, P. Stoltze, *J. Catal.* **221**, 630–649 (2004).
- H. Li, A. Cao, J. K. Nørskov, *ACS Catal.* **11**, 12052–12057 (2021).
- M. O. Ozbek, I. Onal, R. A. Van Santen, *J. Catal.* **284**, 230–235 (2011).
- A. Kokalj, P. Gava, S. de Gironcoli, S. Baroni, *J. Catal.* **254**, 304–309 (2008).
- C. T. Campbell, *J. Catal.* **99**, 28–38 (1986).
- C. J. Chen, J. W. Harris, A. Bhan, *Chemistry* **24**, 12405–12415 (2018).
- A. J. F. Van Hoof, E. A. R. Hermans, A. P. Van Bavel, H. Friedrich, E. J. M. Hensen, *ACS Catal.* **9**, 9829–9839 (2019).
- J. T. Jankowiak, M. A. Barteau, *J. Catal.* **236**, 379–386 (2005).
- M. Huš, A. Hellman, *J. Catal.* **363**, 18–25 (2018).
- A. Hwang, J. Klauke, C. Lizandara-Pueyo, A. Karpov, E. Iglesia, *ChemCatChem* **16**, 1–24 (2023).
- W. Diao, C. D. Digiulio, M. T. Schaal, S. Ma, J. R. Monnier, *J. Catal.* **322**, 14–23 (2015).
- T. Pu, H. Tian, M. E. Ford, S. Rangarajan, I. E. Wachs, *ACS Catal.* **9**, 10727–10750 (2019).
- S. Lincic, M. A. Barteau, *J. Am. Chem. Soc.* **124**, 310–317 (2002).
- S. Wu, B. J. Tatarchuk, A. J. Adamczyk, *Surf. Sci.* **708**, 121834 (2021).
- S. V. Dhalewadikar, E. N. Martinez, A. Varma, *Chem. Eng. Sci.* **41**, 1743–1746 (1986).
- E. A. Carbonio et al., *Chem. Sci.* **9**, 990–998 (2017).
- S. Lincic, M. A. Barteau, *J. Catal.* **214**, 200–212 (2003).
- D. Jingfa, Y. Jun, Z. Shi, Y. Xiaohong, *J. Catal.* **138**, 395–399 (1992).
- J. C. Dellamorte, J. Lauterbach, M. A. Barteau, *Appl. Catal. A Gen.* **391**, 281–288 (2011).
- S. Lincic, J. Jankowiak, M. A. Barteau, *J. Catal.* **224**, 489–493 (2004).
- M. Huš et al., *Angew. Chem. Int. Ed.* **62**, e202305804 (2023).
- M. D. Marcinkowski et al., *ACS Catal.* **7**, 413–420 (2017).
- G. Giannakakis et al., *J. Am. Chem. Soc.* **143**, 21567–21579 (2021).

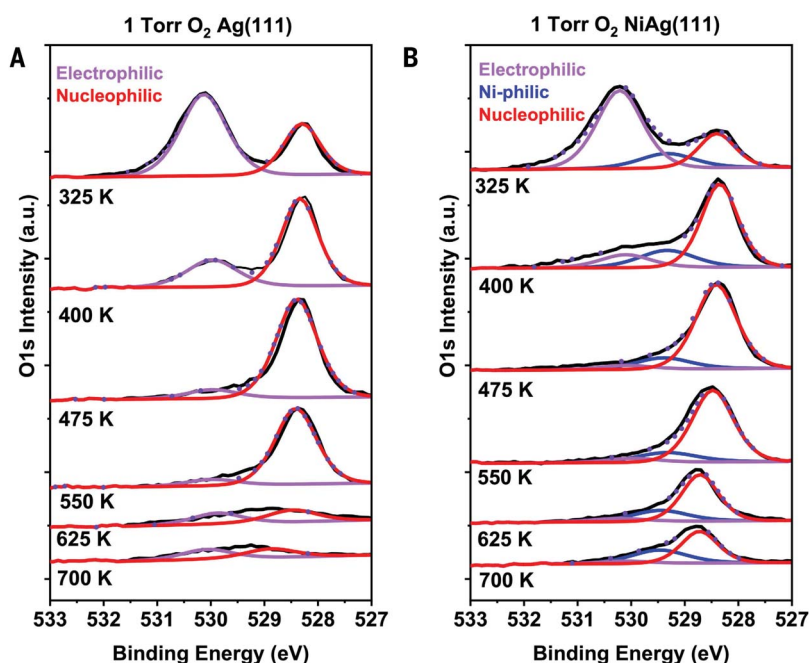


Fig. 4. Electronic structure of oxygen on Ag(111) and NiAg(111) as a function of temperature in 1 Torr O₂. AP-XPS spectra showing a change in oxygen species from primarily electrophilic oxygen (purple, ~ 530.2 eV) to more nucleophilic oxygen (red, ~ 528.5 eV) as the temperature was increased on (A) Ag(111) and (B) $\sim 5\%$ NiAg(111). The Ni-philic O species (529.3 eV) is shown in blue and was only observed for the NiAg sample. O 1s spectra were taken at 760 eV from 325 to 700 K in 1 Torr O₂. The dotted traces represent the combined fits of the oxygen species overlaid with the solid black raw spectra.

28. G. Kyriakou *et al.*, *Science* **335**, 1209–1212 (2012).
29. R. T. Hannagan *et al.*, *Science* **372**, 1444–1447 (2021).
30. M. M. Montemore, M. A. van Spronsen, R. J. Madix, C. M. Friend, *Chem. Rev.* **118**, 2816–2862 (2018).
31. S. R. Bare, K. Griffiths, W. N. Lennard, H. T. Tang, *Surf. Sci.* **342**, 185–198 (1995).
32. C. T. Campbell, *J. Catal.* **94**, 436–444 (1985).
33. A. Klust, R. J. Madix, *Surf. Sci.* **600**, 5025–5040 (2006).
34. W. Hansen, M. Bertolo, K. Jacobi, *Surf. Sci.* **253**, 1–12 (1991).
35. F. P. Netzer, T. E. Madey, *J. Chem. Phys.* **76**, 710–715 (1982).
36. J. E. van den Reijen *et al.*, *J. Catal.* **356**, 65–74 (2017).
37. K. R. Iyer, A. Bhan, *J. Catal.* **420**, 99–109 (2023).
38. B. T. Egelske, W. Xiong, H. Zhou, J. R. Monnier, *J. Catal.* **410**, 221–235 (2022).
39. J. Liu *et al.*, *Catal. Sci. Technol.* **7**, 4276–4284 (2017).
40. X. Gao *et al.*, *Sci. Rep.* **10**, 1365 (2020).
41. P. Christopher, S. Linic, *ChemCatChem* **2**, 78–83 (2010).
42. P. H. Keijzer, J. E. van den Reijen, C. J. Keijzer, K. P. de Jong, P. E. de Jongh, *J. Catal.* **405**, 534–544 (2022).
43. C. J. Keijzer, L. C. J. Smulders, D. Wezendonk, J. W. de Rijk, P. E. de Jongh, *Catal. Today* **428**, 114447 (2024).
44. J. R. Lockemeyer, T. L. Lohr, *ChemCatChem* **15**, e202201511 (2023).
45. V. I. Bukhtiyarov, I. P. Prosvirin, R. I. Kvon, *Surf. Sci.* **320**, L47–L50 (1994).
46. M. A. Peck, M. A. Langell, *Chem. Mater.* **24**, 4483–4490 (2012).
47. K.-H. Dostert, C. P. O'Brien, F. Ivars-Barceló, S. Schauerermann, H. J. Freund, *J. Am. Chem. Soc.* **137**, 13496–13502 (2015).

ACKNOWLEDGMENTS

E.E.H. thanks P. Kress, C. Easton, and A. Daniels for their assistance during AP-XPS experiments at BNL. A.J. thanks J. Perez-Aguilar, J. Hong, S. R. Bare, and D. Sokaras for their assistance during XAS experiments at SSRL. **Funding:** A.J. and P.C. acknowledge primary financial support from the US Department of Energy, BES, Catalysis Science program under contract DE-SC0021124. E.E.H., L.C., and E.C.H.S. acknowledge primary financial support from the US Department of Energy, BES, CPIMS program under contract DE-SC0004738. M.M.M. acknowledges support from Tulane University and the National Science Foundation through grant CHE-2154952. A.S.H., part of Co-ACCESS and part of the SUNCAT Center for Interface Science and Catalysis, is supported by the U.S. Department of Energy, Office of Basic Energy Sciences, Chemical Sciences, Geosciences and Biosciences Division. The use of the Stanford Synchrotron Radiation Lightsource, SLAC National Accelerator Laboratory, is supported by the U.S. Department of Energy, Office of Science, Office of Basic Energy Sciences under contract DE-AC02-76SF00515. Use of the ICP and microscopy equipment in the UCSB MRL Shared Experimental Facilities is acknowledged, which are supported by the MRSEC Program of the National Science Foundation under award DMR 1720256. This research used resources of the 23-ID-2 (IOS) beamline of the National Synchrotron Light Source II, a U.S. Department of Energy (DOE) Office of Science User Facility operated for the DOE Office of Science by Brookhaven National Laboratory under Contract No. DE-SC0012704. High performance computing resources and services were provided by Technology Services at Tulane

University, New Orleans, LA, USA. **Competing interests:** UCSB submitted a US provisional patent (63/392,370, filed on 26 July 2022) and a PCT International patent (PCT/US23/68581, filed on 16 June 2023) entitled “Highly selective catalyst composition for the oxidation of alkenes to Epoxides” on which A.J., P.C., M.M.M., L.C., and E.C.H.S. are listed as inventors. All other authors declare no other competing interests. Author contributions: Conceptualization: M.M.M., E.C.H.S., P.C., and A.J. Investigation: A.J., E.E.H., L.C., A.H., A.S.H., I.W., and M.M.M. Funding acquisition: M.M.M., E.C.H.S., P.C., and I.W. Supervision: M.M.M., E.C.H.S., P.C., and I.W. Writing, review, and editing: A.J., E.C.H.S., P.C., M.M.M., I.W., E.E.H., L.C., A.H., and A.S.H. **Data and materials availability:** All data is available in the main text or the supplementary materials. **License information:** Copyright © 2025 the authors, some rights reserved; exclusive licensee American Association for the Advancement of Science. No claim to original US government works. <https://www.science.org/about/science-licenses-journal-article-reuse>

SUPPLEMENTARY MATERIAL

[science.org/doi/10.1126/science.adt1213](https://doi.org/10.1126/science.adt1213)
Materials and Methods
Supplemental Text
Figs. S1 to S21
Tables S1 to S7
References (48–87)

Submitted 14 September 2024; accepted 8 January 2025
10.1126/science.adt1213